

Continual Learning and Lifting of Koopman Dynamics for Linear Control of Legged Robots

Feihan Li

Abulikemu Abuduweili

Yifan Sun

Rui Chen

Weiye Zhao

Changliu Liu

FEIHANL@ANDREW.CMU.EDU

ABULIKEA@ANDREW.CMU.EDU

YIFANSU2@ANDREW.CMU.EDU

RUIC3@ANDREW.CMU.EDU

WEIYEZHA@ANDREW.CMU.EDU

CLIU6@ANDREW.CMU.EDU

Robotics Institute, Carnegie Mellon University, Pittsburgh, PA 15213, USA

Abstract

The control of legged robots, particularly humanoid and quadruped robots, presents significant challenges due to their high-dimensional and nonlinear dynamics. While linear systems can be effectively controlled using methods like Model Predictive Control (MPC), the control of nonlinear systems remains complex. One promising solution is the Koopman Operator, which approximates nonlinear dynamics with a linear model, enabling the use of proven linear control techniques. However, achieving accurate linearization through data-driven methods is difficult due to issues like approximation error, domain shifts, and the limitations of fixed linear state-space representations. These challenges restrict the scalability of Koopman-based approaches. This paper addresses these challenges by proposing a continual learning algorithm designed to iteratively refine Koopman dynamics for high-dimensional legged robots. The key idea is to progressively expand the dataset and latent space dimension, enabling the learned Koopman dynamics to converge towards accurate approximations of the true system dynamics. Theoretical analysis shows that the linear approximation error of our method converges monotonically. Experimental results demonstrate that our method achieves high control performance on robots like Unitree G1/H1/A1/Go2 and ANYmal D, across various terrains using simple linear MPC controllers. This work is the first to successfully apply linearized Koopman dynamics for locomotion control of high-dimensional legged robots, enabling a scalable model-based control solution.

Keywords: Koopman Operator Theory, Model Predictive Control, Legged Robots, Continual Learning

1. Introduction

The control of legged robots has garnered increasing attention due to the growing potential of humanoid and quadruped robots in real-world applications. However, the task is challenging and is complicated by the high-dimensional and nonlinear dynamics inherent in legged systems. Existing methods for controlling nonlinear systems exhibit a trade-off between emphasizing controller synthesis and emphasizing modeling, and can be categorized into model-free and model-based approaches. Model-free methods directly derive the control law without explicitly modeling the system dynamics. Reinforcement learning (RL) is the representative example, demonstrating notable success in controlling legged robots in real-world applications [Song et al. \(2021\)](#); [Haarnoja et al. \(2018\)](#); [Zhao et al.](#); [He et al. \(2024\)](#); [Lee et al. \(2020\)](#); [He et al. \(2024\)](#); [Fu et al. \(2024\)](#); [Luo et al. \(2023\)](#). Despite their strong performance, model-free control laws are often highly task-specific and require retraining or fine-tuning when adapting to new capabilities.

In contrast, model-based approaches decouple the modeling of system dynamics from the realization of task objectives, enabling more efficient adaptation to new tasks. The models used in these approaches can be categorized as: original nonlinear models, locally linearized nonlinear models, globally linearized nonlinear models, with increasing modeling complexity and decreasing control complexity. For direct control of nonlinear models, [Yi et al. \(2024\)](#) is available for controlling legged system with sampling-based MPC, while [Kazemi et al. \(2013\)](#) applies robust backstepping control to quadruped robots. Local linearization methods, iLQR [Li and Todorov \(2004\)](#) and NMPC [Grüne et al. \(2017\)](#) often combine analytical [Sotaro Katayama and Tazaki \(2023\)](#); [Zhu et al. \(2024\)](#) or learned models [Nagabandi et al. \(2017\)](#); [Liu et al. \(2023\)](#) with complex controllers. A promising alternative is employing Koopman Operator Theory to construct globally linearized nonlinear models of legged systems and enabling the use of simpler controller, like MPC, with performance guarantees. Although Koopman-based methods have proven effective in legged robot tasks such as motion planning [Kim et al. \(2024a\)](#) and gait prediction [Krolicki et al. \(2022\)](#), no attempts have been made to directly control legged systems.

When deriving the Koopman Operator analytically is ineffective, our method leverages a data-driven approach that minimizes the need for expert knowledge while ensuring strong generalizability. Within data-driven approach, recent methods have applied Koopman dynamics to high-level motion planning [Kim et al. \(2024a\)](#); [Lyu et al. \(2023\)](#). However, these methods still rely on end-to-end optimization toward task objectives, limiting the generalizability. In contrast, [Shi and Meng \(2022\)](#); [Korda and Mezić \(2018b\)](#); [Mamakoukas et al. \(2021\)](#) focus on obtaining accurate Koopman approximations for low-level control, but their applicability is limited to low-dimensional systems [Shi et al. \(2024\)](#). Controlling high-dimensional nonlinear systems with Koopman is challenging due to (a) imperfect approximations and (b) domain shifts from limited state transition data that only spans a subspace of the full state space. Approximation errors make the system sensitive to poorly-modeled dynamics, while domain shifts cause failures under perturbations.

To address the challenges, we propose a continual learning algorithm designed to progressively learn Koopman dynamics for high-dimensional legged robots. The central idea is to iteratively expand the dataset effectively while increasing the latent space dimension to accommodate the growing dataset. Upon convergence, the accumulated dataset spans a state space naturally within which the learned Koopman dynamics exhibit high control performance. Additionally, we provide a theoretical analysis of the convergence of the learned Koopman dynamics towards the true dynamics, validating the effectiveness of our approach. Experimental results demonstrate that our Koopman dynamics minimize linearization error after only a few iterations and enable effective locomotion control for legged robots using simple Model Predictive Control (MPC) controllers. In summary, our contributions are:

1. An iterative continual learning algorithm designed to mitigate approximation errors and domain shifts, achieving high approximation accuracy in just a few iterations, with a theoretical guarantee of error convergence.
2. This is the first work that achieves effective locomotion control for high-dimensional legged robots using linearized system dynamics with simple MPC controllers, with validation on the most advanced legged robots across various terrains.

2. Problem Formulation

2.1. Preliminary: Koopman Operator Theory

Koopman Operator Theory offers a powerful framework for analyzing nonlinear dynamical systems by mapping them into equivalent linear systems in an infinite-dimensional latent space. Consider the discrete-time nonlinear autonomous system $s_{t+1} = f(s_t)$, where $s_t \in \mathcal{S}$ represents the state. Koopman operator theory introduces the embedding function $\phi : \mathcal{S} \rightarrow \mathcal{O}$ to map the original state space \mathcal{S} to an infinite dimensional latent space \mathcal{O} . In this latent space, the dynamics become linear through the Koopman Operator \mathcal{K} :

$$\mathcal{K}\phi(s) = \phi(f(s)) \quad (1)$$

Consider a non-autonomous dynamical system with control input $u_t \in \mathcal{U} \subset \mathbb{R}^{m'}$ and system state $x_t \in \mathcal{X} \subset \mathbb{R}^{n'}$, given by $x_{t+1} = f(x_t, u_t)$. The Koopman Operator transforms the system dynamics into a linear form.

$$\mathcal{K}\phi(x_t, u_t) = \phi(f(x_t, u_t)) = \phi(x_{t+1}) \quad (2)$$

In practice, we approximate the Koopman operator by constraining latent space to a finite-dimensional vector space. For a control dynamics system, a common strategy is to define the embedding function as $\phi(x_t, u_t) = [g(x_t); u_t]$, where $g : \mathbb{R}^{n'} \rightarrow \mathbb{R}^n$ is a state embedding function. Using a matrix representation $K = \begin{bmatrix} A \in \mathbb{R}^{n \times n} & B \in \mathbb{R}^{n \times m'} \\ C \in \mathbb{R}^{m' \times n} & D \in \mathbb{R}^{m' \times m'} \end{bmatrix}$ to approximate Koopman operator \mathcal{K} , and in conjunction with eq. (2), we obtain linear dynamics in the lifted space. We focus on the state evolution, then we have

$$g(x_{t+1}) = Ag(x_t) + Bu_t \quad (3)$$

To preserve state information with clear semantics [Shi and Meng \(2022\)](#), and avoid the case of degeneration, such as cases where $A = B = 0$ and $g(x) \equiv 0$, we concatenate the original state with the neural network embedding to define the latent state z_t as $z_t = g(x_t) = [x_t, g'(x_t)]^\top$, where $g' : \mathbb{R}^{n'} \rightarrow \mathbb{R}^{n-n'}$ is a parameterized neural network. This approach allows us to retrieve the original state using a linear transformation.

$$x_{t+1} = Pz_{t+1} = Pg(x_{t+1}), \quad P = [I_{n' \times n'}, \mathbf{0}_{n' \times (n-n')}] \in \mathbb{R}^{n' \times n} \quad (4)$$

This formulation supports solving constrained problems, such as obstacle avoidance, without compromising the system's linear properties. Additionally, we use an end-to-end training approach for both the embedding function and the Koopman operator, parameterized as $\mathcal{T} \doteq (g, A, B)$.

2.2. Linear Model Predictive Control

The linear evolution in the latent space we obtain is well-suited for linear control methods, which are both simple and effective. In our high-dimensional legged robot control tasks, we employ a linear MPC algorithm as the controller π_{mpc} , thus the problem can be easily solved by Quadratic Programming (QP). The optimization formulation at time step t is as follows:

$$\begin{aligned} \min_{u_{t:t+H-1}} \quad & \|Pz_{t:t+H-1} - x_{t:t+H-1}^*\|_Q^2 + \|u_{t:t+H-1}\|_R^2 + \|Pz_{t+H} - x_{t+H}^*\|_F^2 \\ \text{s.t.} \quad & z_{t+k+1} = Az_{t+k} + Bu_{t+k}, \quad u_{t+k} \in [u_{min}, u_{max}], \quad \forall k = 0, \dots, H-1 \end{aligned} \quad (5)$$

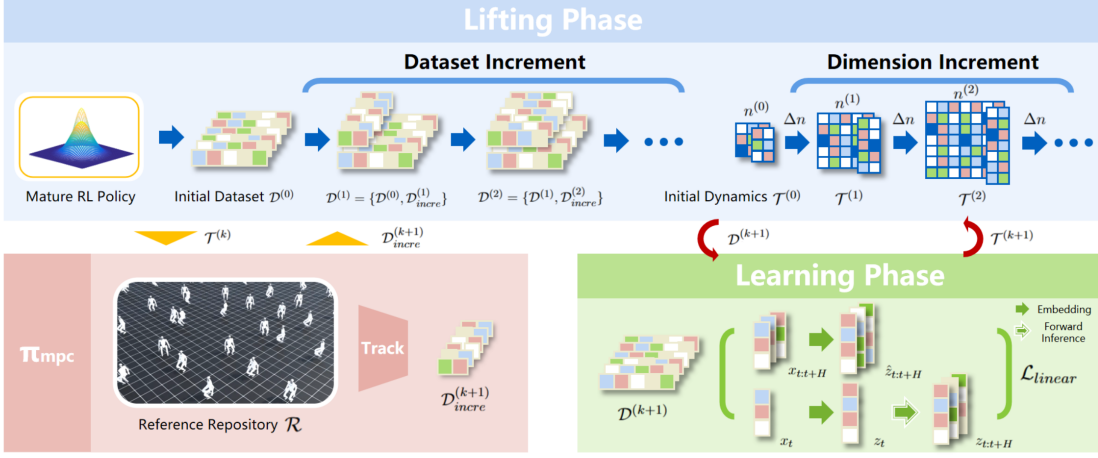


Figure 1: Overview of Incremental Koopman Algorithm

where H denotes the horizon length, $x_{t:t+H}^*$ represents the reference trajectory, Q, R, F are cost matrices and $\|x\|_Q^2$ is defined as $x^T Q x$. The range $[u_{min}, u_{max}]$ specifies the valid interval for control inputs. The first constraint ensures adherence to the learned dynamics in the latent space, while the second constraint bounds control signals within the valid region. It is worth noting that, unlike learning-based methods, dynamics do not inherently encode gait features, making full-body reference tracking essential for maintaining stable and reasonable movement patterns.

2.3. Legged Robot System

As demonstrated in [Wieber et al. \(2016\)](#), legged robot systems inherently possess the following characteristics: (i) discontinuities resulting from mode transitions, (ii) sensitivity to noisy control inputs while maintaining balance, and (iii) failure situations that are often irrecoverable.

Existing Koopman-based methods primarily focus on low-dimensional continuous systems with fixed contact modes [Shi and Meng \(2022\)](#), where the dynamics are continuous and easier to fit. However, when applied to high-dimensional hybrid legged systems, the complex and diverse contact modes introduce significant discontinuities, greatly complicating the modeling process. Moreover, these existing Koopman methods, which exhibit considerable approximation errors and limited latent subspace [Han et al. \(2023\)](#), render hybrid legged systems prone to irrecoverable failures caused by unmodeled dynamics and external perturbations. To overcome these challenges, we developed an algorithm that accurately and robustly models dynamics through continual learning and lifting, effectively expanding a resilient latent subspace.

3. Incremental Koopman Algorithm

3.1. Initialization and Increment of Dataset

Initial Data Collector. Mainstream methods, as demonstrated in [Shi and Meng \(2022\)](#); [Shi et al. \(2024\)](#), typically collect training data by randomizing the control input and gathering state transition pairs, which is sufficient for low-dimensional continuous systems. However, when applied to high-dimensional hybrid systems, such as legged robots, this data collection method is insufficient due to

the complex interactions involved in contact. Thus, inspired by [Rudin et al. \(2022\)](#); [Schulman et al. \(2017b\)](#), we leverage Proximal Policy Optimization (PPO) policy as data collector to build initial dataset $\mathcal{D}^{(0)}$ and reference repository \mathcal{R} , ensuring stable gait and consistent contact modes with the ground, which is crucial for learning a meaningful latent subspace.

Increment Data Collector. To address the challenges of considerable approximation errors and limited latent subspace introduced in section 2.3, it is essential that the learned Koopman dynamics can infer failure scenarios, such as falling, under specific gait and contact modes, without modifying the environment by applying external forces. To achieve this, we leverage the MPC controller introduced in Section 2.2 to track diverse references in \mathcal{R} , collecting failed tracking data \mathcal{D}_{incre} to naturally expand the dataset, thereby enhancing the robustness and reliability of the latent subspace. To validate the effectiveness of our dataset expansion, we conduct experiments in Section 4.4 and visualize the results in Figure 5.

3.2. Training with Given Data

Based on the base Koopman framework introduced in Section 2.1, our primary goal is to learn the embedding function g and the Koopman operators A, B end-to-end. To achieve this, we employ a discounted k-step prediction loss to enhance long-horizon prediction capabilities which is crucial for MPC control. Given a set of trajectory data $\{x_{t:t+H}; u_{t:t+H-1}\}$, real latent trajectories can be computed as $\{z_{t:t+H} = g(x_{t:t+H})\}$. At the same time, predicted latent trajectories can be obtained through inference: $\{\hat{z}_{t:t+H} | \hat{z}_t = z_t, \hat{z}_{t+h} = A\hat{z}_{t+h-1} + Bu_{t+h-1}, h = 1, 2, \dots, H\}$. Thus the loss function is defined as:

$$\mathcal{L}_{koopman} = \frac{1}{H} \sum_{h=1}^H \gamma^h \left(\underbrace{\|\hat{z}_{t+h} - z_{t+h}\|^2}_{\mathcal{L}_{linear}} + \alpha \underbrace{\|\hat{x}_{t+h} - x_{t+h}\|^2}_{\mathcal{L}_{recon}} \right) \quad (6)$$

where $\hat{x}_{t:t+H} = P\hat{z}_{t:t+H}$, α is the weight of \mathcal{L}_{recon} and γ is the discount factor. Here \mathcal{L}_{linear} focuses on the linearization effect, while \mathcal{L}_{recon} addresses on the reconstruction effect. Thus can derive dynamics $\mathcal{T}^{(k)} \doteq (g_{n^{(k)}}^{(k)}, A_{n^{(k)}}^{(k)}, B_{n^{(k)}}^{(k)})$ for dataset $\mathcal{D}^{(k)}$, here $n^{(k)}$ represents the latent space dimension of iteration k .

3.3. Continual Learning and Lifting

As shown in the overall pipeline in Figure 1, the incremental Koopman algorithm begins with the initial dynamics $\mathcal{T}^{(0)}$ trained on the initial dataset $\mathcal{D}^{(0)}$. During the lifting phase, we use the increment data collector introduced in Section 3.1 to gather the incremental dataset $\mathcal{D}^{(1)incre}$, which is then used to augment the initial dataset, forming $\mathcal{D}^{(1)} = \mathcal{D}^{(0)} \cup \mathcal{D}^{(1)incre}$. Simultaneously, to accommodate the growing dataset, the latent space dimension is updated as $n^{(1)} = n^{(0)} + \Delta n$, where Δn is a hyperparameter chosen based on the trade-off between computational complexity, performance gain, and the requirement $m = \Omega(n \log(n))$ introduced in Section 3.4, where m denotes the dataset size.

In the learning phase, we utilize the loss introduced in Section 3.2 to obtain $\mathcal{T}^{(1)} = (g_{n^{(1)}}^{(1)}, A_{n^{(1)}}^{(1)}, B_{n^{(1)}}^{(1)})$. This process is repeated until the survival steps T_{sur} under MPC control with dynamics $\mathcal{T}^{(k)}$ cease to show improvement over $\mathcal{T}^{(k-1)}$. Please check Algorithm 1 for details. Through the continual learning and lifting process, the linear dynamics of the latent subspace, enhanced using the incremental dataset, improve in predicting failure scenarios under specific movement patterns. This is

crucial for the MPC controller to make reliable decisions, significantly reducing approximation errors and establishing robust linear latent dynamics. To validate our claim, a series of experiments are conducted in Section 4.

3.4. Theoretical analysis

The core premise established in [Korda and Mezić \(2018a,b\)](#) is that the learned Koopman operator K is the L_2 projection of the true Koopman operator \mathcal{K} on the span of ϕ_1, \dots, ϕ_n with respect to the empirical measure on the samples, where $\Phi(s) = [\phi_1(s), \dots, \phi_n(s)]$ are embedding functions. Our theoretical analysis introduces the convergence rate of the algorithm under additional assumptions, further expanding on the existing knowledge base. Benefiting from the decomposition of total error as sampling error $\epsilon_{\text{samp}}(n, m)$ and projection error $\epsilon_{\text{proj}}(n)$, we derive the following theorem:

Theorem 1. *Under the assumptions of 1) data samples s_1, \dots, s_m are i.i.d distributed; 2) the latent state is bounded, $\|\phi(s)\| < \infty$; 3) the embedding functions ϕ_1, \dots, ϕ_n are orthogonal (independent). (a) The learned Koopman operator converges to the true Koopman Operator:*

$$\lim_{m=\Omega(n \ln(n)), n \rightarrow \infty} K \rightarrow \mathcal{K}. \quad (7)$$

(b) *Assuming additional conditions: 4) The eigenvalues of the Koopman operator \mathcal{K} decay sufficiently fast, for instance, $|\lambda_i| \leq \frac{C}{i^\alpha}$ for some constant $C > 0, \alpha > \frac{1}{2}$. 5) The embedding functions $\Phi(\cdot) = [\phi_1, \dots, \phi_n]^\top$ correspond to the first n eigenfunctions of \mathcal{K} associated with the largest eigenvalues in magnitude. The convergence rate of the combined error is given by:*

$$\text{error} \leq \mathcal{O}\left(\sqrt{\frac{\ln(n)}{m}}\right) + \mathcal{O}\left(\frac{1}{n^{\alpha-\frac{1}{2}}}\right). \quad (8)$$

For comprehensive proof and further details, please refer to appendix D.

4. Experiments

In our experiments, we evaluate the proposed method by addressing the following questions:

Q1 Does the learned Koopman Dynamics from algorithm 1 achieve better state prediction performance compared to baselines?

Q2 Does our approach, combining learned Koopman dynamics with MPC control, achieve superior tracking performance relative to baselines?

Q3 Is the continual expansion of the dataset size in our proposed method effective?

Q4 Is the continual increase in the dimensions of the latent state beneficial?

4.1. Experiment Setup

Task settings. Our experiments use IsaacLab [Mittal et al. \(2023\)](#) as the simulation platform, the most advanced simulator offering comprehensive and flexible support for a wide range of robots and environments. Five different legged robots are included in our experiments: (i) **ANYmal-D:** (Figure 8(a)) A quadruped robot ($\mathcal{U} \subseteq \mathbb{R}^{12}$) designed by ANYbotics. (ii) **Unitree-A1:** (Figure 8(b)) A quadruped robot ($\mathcal{U} \subseteq \mathbb{R}^{12}$) designed by Unitree. (iii) **Unitree-Go2:** (Figure 8(b)) A quadruped robot ($\mathcal{U} \subseteq \mathbb{R}^{12}$) designed by Unitree. (iiiv) **Unitree-H1:** (Figure 8(b)) A Humanoid ($\mathcal{U} \subseteq \mathbb{R}^{19}$) designed by Unitree. (v) **Unitree-G1:** (Figure 8(b)) A Humanoid ($\mathcal{U} \subseteq \mathbb{R}^{23}$) designed by Unitree.

Furthermore, two different types of terrain are considered, including (i) **Flat:** (Figure 8(f)) flat terrain. (ii) **Rough:** (Figure 8(g)) rough terrain with random surface irregularities, where the height follows a uniform distribution between 0.005 and 0.025, and the minimum height variation is 0.005 (in m). All test suites are based on the task **Walk:** tracking a velocity command with uniformly sampled heading direction, x-axis linear velocity, and y-axis linear velocity. Considering these settings, we design 7 test suites with 5 types of legged robots and 2 types of terrain, which are summarized in Table 3. We name these test suites as $\{\text{Terrain}\}-\{\text{Make}\}-\{\text{Model}\}$.

Comparison Group. We compare Incremental Koopman algorithm with state-of-the-art Koopman-based algorithms (i) Deep KoopmanU with Control (DKUC, Shi and Meng (2022)) algorithm, (ii) Deep Koopman Affine with control (DKAC, Shi and Meng (2022)) algorithm, (iii) Neural Network Dynamics Model (NNDM, Nagabandi et al. (2017); Liu et al. (2023)) with MPC (iiiv) Deep Koopman Reinforcement Learning (DKRL, Song et al. (2021)). For all experiments, we take the best algorithm-specific parameters mentioned in the original paper and keep the common parameters as the same.

Metrics. We introduce the following metrics to evaluate the tracking ability of our algorithm: (i) **Prediction-based:** we leverage k-step prediction error $E_{pre}(k) \doteq \frac{1}{kn'} \sum_{t=1}^k \|x_t - x_t^*\|_1$ ($x_0 = x_0^*$) generally used for measuring prediction ability of given dynamics. (ii) **Pose-based:** To evaluate tracking accuracy, we evaluate Joint-relative mean per-joint position error (E_{JrPE}), Joint-relative mean per-joint velocity error (E_{JrVE}), Joint-relative mean per-joint acceleration error (E_{JrAE}), Root mean position error (E_{RPE}), Root mean orientation error (E_{ROE}), Root mean linear velocity error (E_{RLVE}) and Root mean angular velocity error (E_{RLAE}). Check Appendix E.4 for detailed equations. (iii) **Physics-based:** Considering the easy-to-fail feature of legged robots, for the same reference repository \mathcal{R} , we evaluate the average survival simulation time step T_{Sur} (set 200 as upper bound, simulation frequency is 50Hz) for each algorithms, deeming tracking unsuccessful when E_{JrPE} is larger than ϵ_{fail} . Check Table 3 for details.

State. The system state $x_t \doteq \begin{cases} (j_t, \dot{j}_t, p_t^z, \dot{p}_t, \dot{r}_t), & \text{for humanoid} \\ (j_t, \dot{j}_t, p_t^z, \dot{p}_t, r_t, \dot{r}_t), & \text{for quadruped robot} \end{cases}$ of dynamics and controller includes the DoF position j_t and DoF velocity \dot{j}_t in local coordinates, root height p_t^z , 3D root linear velocity p_t , 4D root orientation r_t (optional for humanoid and represented as a quaternion), and 3D root angular velocity \dot{r}_t in world coordinates. All of the aforementioned quantities are normalized to follow a standard Gaussian distribution, $\mathcal{N}(0, 1)$, in order to eliminate inconsistencies in the scale of different physical quantities.

Control Input and Low-level Controller. We use a proportional-derivative (PD) controller at each DoF of the legged robots as the low-level controller. Thus, the control input u_t determined by the MPC serves as the joint target, denoted as $j_t^d = u_t$. The torque applied to each joint is given by $\tau_t = k^p \circ (j_t^d - j_t) - k^d \circ \dot{j}_t$, where k^p and k^d are the proportional and derivative gains, respectively. The low-level controller operates at a frequency of 200 Hz, with a decimation factor of 4.

4.2. K-step Prediction Error

To demonstrate the superiority of our algorithms, we evaluate the k-step prediction performance across the seven test suites mentioned above. Specifically, we set k to $[1, 3, 6, 9, 12, 15]$ and compute $E_{pre}(k)$ for each algorithm, subsequently plotting the results in Figure 2. The results highlight our algorithm’s exceptional capability to achieve low prediction errors, even for long prediction horizons in highly nonlinear and complex tasks, a feat challenging for other algorithms within our comparison

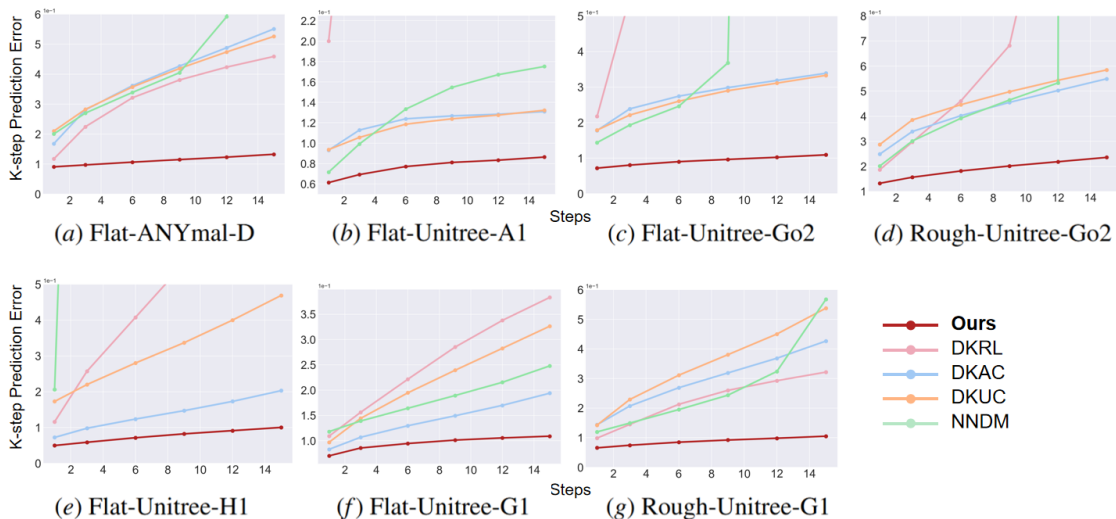


Figure 2: Comparison results of k-step prediction error in our test suites.

group. In Figures 3(c) to 3(e), it is evident that the NNDM-based method and DKRL struggle to avoid the accumulation of explosive errors as the horizon length k increases, whereas our algorithm remains stable, exhibiting only a negligible increase in error. Although the advanced Koopman frameworks DKAC and DKUC can maintain a relatively stable rate of loss increase, they are unable to effectively infer the boundary cases of complex robot motions due to the limitations of subspace modeling in the latent space. This limitation is further confirmed by their poor performance in noisy and complex tracking experiments, as discussed in Section 4.3. Results above answer **Q1**.

4.3. Tracking Performance



Figure 3: Visualization of tracking performance on Flat-Unitree-G1

To demonstrate our sharp lead in the tracking tasks, we add uniform noise ranging from $[-0.05, 0.05]$ to all references in \mathcal{R} to create noisy reference repository $\hat{\mathcal{R}}$, and parallelly track $3e3$ references in $\hat{\mathcal{R}}$ for 200 steps to present our tracking performance in Table 1, which records the average tracking metrics discussed in Section 4.1. More details are in Appendix E.5.

Compared to other algorithms, our approach demonstrates (i) high T_{Sur} that approach the upper bound of 200, (ii) accurate and continuous tracking capabilities at the joint level, and (iii) the ability to sustain global tracking while maintaining balance and stability. All metrics measured for our algorithm are significantly lower than those of others, indicating that competing algorithms fail to track correctly and tend to fall after only a few attempts. In contrast, we maintain efficient and

Synthesised Tracking Metrics								
Algorithm	Joint-relative ↓			Root-relative ↓				Survival ↑
	E_{JrPE}	E_{JrVE}	E_{JrAE}	E_{RPE}	E_{ROE}	E_{RLVE}	E_{RAVE}	T_{Surv}
Ours	0.0316	0.5866	37.1446	0.1035	0.0553	0.1120	0.3007	183.5074
DKRL	0.0831	1.1014	67.5660	0.3291	0.1580	0.2150	0.5441	117.7829
DKAC	0.1816	2.0694	117.5515	0.3955	0.2749	0.2888	0.9143	25.0254
DKUC	0.1576	1.0828	50.5745	0.2934	0.1989	0.2252	0.5559	82.4620
NNDM	0.1439	2.2020	127.4524	0.4334	0.2506	0.2996	0.8536	35.4709

Table 1: The average tracking metrics evaluated for each algorithm across all 7 test suites.

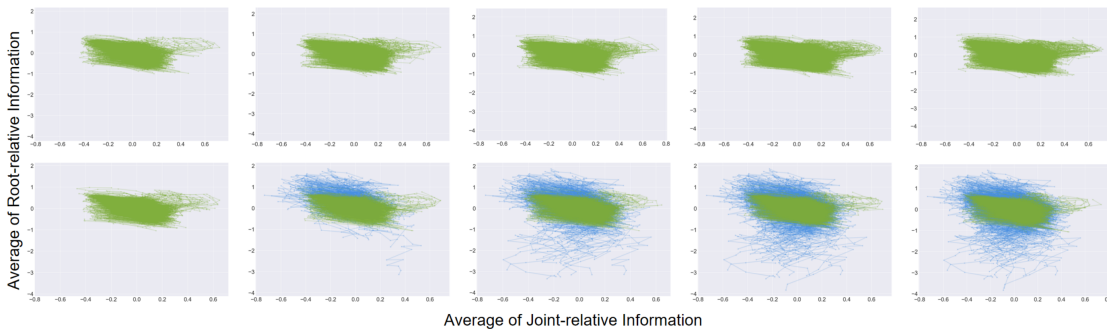


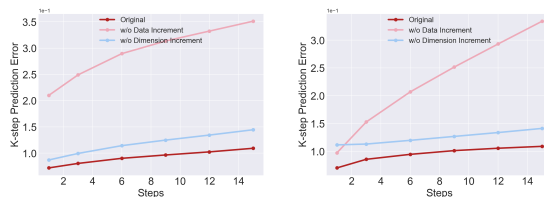
Figure 5: Visualization of the data distribution by plotting the means of the joint-relative and root-relative states. The first row illustrates the dataset expansion achieved using an RL policy, while the second row shows the results from applying our algorithm for dataset expansion.

accurate tracking while exhibiting a steady walking gait. These results highlight our algorithm’s ability to infer corner cases during tracking, benefiting from the continual learning and lifting process described in Algorithm 1. Meanwhile, others struggle to achieve the correct poses and gait when faced with falling or sticking on the ground. It is worth noting that we set 200 as the upper bound for T_{Surv} , suggesting that many test cases are still robust enough to enable tracking for increasingly longer steps.

Although DKRL and DKUC achieve a relatively high T_{Surv} , their E_{JrPE} and E_{RPE} are 2 to 5 times higher than ours, which indicate that their metrics include short clips of failure situations, whereas our algorithm maintains robust tracking even until the end of recording, demonstrating our superiority in steady tracking with extremely low error. As for DKAC and NNDM, they exhibit short inference capabilities and sensitivity to the corners of the dynamics distribution, making them prone to failure, especially when most of the failing situations are unrecoverable for legged robot. As shown in Figure 3, uncoverable failure ends tracking process, which answers **Q2**.

4.4. Ablation on Dataset Increment

For the ablation study on dataset increment, we select the tasks Flat-Unitree-Go2 and Flat-Unitree-G1 to investigate the influence of dataset increment techniques. As illustrated in Table 2



(a) Flat-Unitree-Go2

(b) Flat-Unitree-G1

9 Figure 4: K-step prediction error comparison of ablation on dimension and dataset increment.

Average Tracking Metrics of Flat-Unitree-Go2 and Flat-Unitree-G1								
Algorithm	Joint-relative ↓			Root-relative ↓				Survival ↑
	E_{JrPE}	E_{JrVE}	E_{JrAE}	E_{RPE}	E_{ROE}	E_{RLVE}	E_{RAVE}	T_{Sur}
Original	0.0283	0.6052	40.5622	0.0886	0.0390	0.0966	0.2588	187.8470
w/o Data.I.	0.2052	1.5197	65.2227	0.3487	0.2467	0.2747	0.6281	52.5400
w/o Dim.I.	0.1180	1.1679	63.2691	0.2546	0.1897	0.2171	0.5725	101.1310

Table 2: The average tracking metrics evaluated for the ablation studies. ‘w/o Data.I.’ and ‘w/o Dim.I.’ indicate the performance of the original method without data increment and dimension increment techniques, respectively

and fig. 4, we observe that the k-step prediction error increases rapidly with the number of steps, indicating a lack of inferencing capability when the dynamics encounter corner cases due to insufficient modeling of the latent space’s subspace. Additionally, E_{JrPE} is nearly seven times higher than that of the original method, reflecting the prevalence of failure situations. The low survival steps T_{Sur} further support this insight. In contrast, the original algorithm Algorithm 1 maintains extraordinary tracking ability and loss control, demonstrating the effectiveness of dataset enlargement. In addition, we visualize the data enlargement process in Figure 5. The results indicate that the dataset expansion using the RL policy is ineffective, as it produces repetitive data, while our algorithm demonstrates effective dataset expansion. Therefore, the dataset increment technique highlights the importance of modeling a robust subspace and ensuring accurate inferencing, addressing Q3.

4.5. Ablation on Dimension Increment

To conduct the ablation study on dimension increment, we select the same test suites mentioned in Section 4.4. As shown in Figure 4, the k-step prediction error remains steady and relatively low, similar to the original methods, benefiting from the continual increment of the dataset to model the subspace. However, as indicated in Table 2, although the algorithm without dimension increment outperforms the algorithm without data increment, its tracking performance still falls significantly short of the original method. This suggests that a low latent space dimension fails to model robust dynamics strong enough to resist unseen noise during simulation. Furthermore, the lack of inferencing capability highlights its shortcomings in linearization and generalization. Thus, the dimension increment technique emphasizes the importance of modeling robust and general sub-dynamics, addressing Q4.

5. Conclusion and Future Works

By progressively expanding the dataset and latent subspace, our method ensures convergence of linearization errors and enables accurate approximations of the system dynamics. Experimental results show that the approach achieves high control performance with simple MPC controllers on various tasks after just a few iterations. This work represents the first successful application of linearized Koopman dynamics to locomotion control of legged robots, offering a scalable and model-based control solution. In the future, we will implement our algorithm in safety problems and real robotic systems.

References

- Abulikemu Abuduweili and Changliu Liu. Online model adaptation with feedforward compensation. In *Conference on Robot Learning*, pages 3687–3709. PMLR, 2023.
- Hongyi Chen, Abulikemu Abuduweili, Aviral Agrawal, Yunhai Han, Harish Ravichandar, Changliu Liu, and Jeffrey Ichnowski. Korol: Learning visualizable object feature with koopman operator rollout for manipulation. *arXiv preprint arXiv:2407.00548*, 2024.
- Thor I Fossen and Aslaug Grovlen. Nonlinear output feedback control of dynamically positioned ships using vectorial observer backstepping. *IEEE transactions on control systems technology*, 6(1):121–128, 1998.
- Zipeng Fu, Qingqing Zhao, Qi Wu, Gordon Wetzstein, and Chelsea Finn. Humanplus: Humanoid shadowing and imitation from humans, 2024. URL <https://arxiv.org/abs/2406.10454>.
- Lars Grüne, Jürgen Pannek, Lars Grüne, and Jürgen Pannek. *Nonlinear model predictive control*. Springer, 2017.
- Tuomas Haarnoja, Aurick Zhou, Pieter Abbeel, and Sergey Levine. Soft actor-critic: Off-policy maximum entropy deep reinforcement learning with a stochastic actor. In *International conference on machine learning*, pages 1861–1870. PMLR, 2018.
- Yunhai Han, Mandy Xie, Ye Zhao, and Harish Ravichandar. On the utility of koopman operator theory in learning dexterous manipulation skills. In *Conference on Robot Learning*, pages 106–126. PMLR, 2023.
- Kaiming He, Xiangyu Zhang, Shaoqing Ren, and Jian Sun. Deep residual learning for image recognition, 2015. URL <https://arxiv.org/abs/1512.03385>.
- Tairan He, Zhengyi Luo, Wenli Xiao, Chong Zhang, Kris Kitani, Changliu Liu, and Guanya Shi. Learning human-to-humanoid real-time whole-body teleoperation. *arXiv preprint arXiv:2403.04436*, 2024.
- Eurika Kaiser, J Nathan Kutz, and Steven L Brunton. Data-driven approximations of dynamical systems operators for control. *The Koopman operator in systems and control: concepts, methodologies, and applications*, pages 197–234, 2020.
- Hamed Kazemi, Vahid Johari Majd, and Majid M. Moghaddam. Modeling and robust backstepping control of an underactuated quadruped robot in bounding motion. *Robotica*, 31(3):423–439, 2013. doi: 10.1017/S0263574712000458.
- Jeonghwan Kim, Yunhai Han, Harish Ravichandar, and Sehoon Ha. Learning koopman dynamics for safe legged locomotion with reinforcement learning-based controller. *arXiv preprint arXiv:2409.14736*, 2024a.
- Jin Sung Kim, Ying Shuai Quan, and Chung Choo Chung. Uncertainty quantification of autoencoder-based koopman operator. In *2024 American Control Conference (ACC)*, pages 4631–4636. IEEE, 2024b.

- Milan Korda and Igor Mezić. On convergence of extended dynamic mode decomposition to the koopman operator. *Journal of Nonlinear Science*, 28:687–710, 2018a.
- Milan Korda and Igor Mezić. Linear predictors for nonlinear dynamical systems: Koopman operator meets model predictive control. *Automatica*, 93:149–160, 2018b.
- Alexander Krolicki, Dakota Rufino, Andrew Zheng, Sriram S.K.S Narayanan, Jackson Erb, and Umesh Vaidya. Modeling quadruped leg dynamics on deformable terrains using data-driven koopman operators. *IFAC-PapersOnLine*, 55(37):420–425, 2022. ISSN 2405-8963. doi: <https://doi.org/10.1016/j.ifacol.2022.11.219>. URL <https://www.sciencedirect.com/science/article/pii/S2405896322028622>. 2nd Modeling, Estimation and Control Conference MECC 2022.
- Joonho Lee, Jemin Hwangbo, Lorenz Wellhausen, Vladlen Koltun, and Marco Hutter. Learning quadrupedal locomotion over challenging terrain. *Science robotics*, 5(47):eabc5986, 2020.
- Weiwei Li and Emanuel Todorov. Iterative linear quadratic regulator design for nonlinear biological movement systems. In *First International Conference on Informatics in Control, Automation and Robotics*, volume 2, pages 222–229. SciTePress, 2004.
- Zhizhong Li and Derek Hoiem. Learning without forgetting. *IEEE transactions on pattern analysis and machine intelligence*, 40(12):2935–2947, 2017.
- Ziang Liu, Gengeng Zhou, Jeff He, Tobia Marcucci, Li Fei-Fei, Jiajun Wu, and Yunzhu Li. Model-based control with sparse neural dynamics, 2023. URL <https://arxiv.org/abs/2312.12791>.
- Zhengyi Luo, Jinkun Cao, Kris Kitani, Weipeng Xu, et al. Perpetual humanoid control for real-time simulated avatars. In *Proceedings of the IEEE/CVF International Conference on Computer Vision*, pages 10895–10904, 2023.
- Xubo Lyu, Hanyang Hu, Seth Siriya, Ye Pu, and Mo Chen. Task-oriented koopman-based control with contrastive encoder. In *Conference on Robot Learning*, pages 93–105. PMLR, 2023.
- Arun Mallya and Svetlana Lazebnik. Packnet: Adding multiple tasks to a single network by iterative pruning. In *Proceedings of the IEEE conference on Computer Vision and Pattern Recognition*, pages 7765–7773, 2018.
- Giorgos Mamakoukas, Maria L Castano, Xiaobo Tan, and Todd D Murphey. Derivative-based koopman operators for real-time control of robotic systems. *IEEE Transactions on Robotics*, 37(6):2173–2192, 2021.
- Mayank Mittal, Calvin Yu, Qinxu Yu, Jingzhou Liu, Nikita Rudin, David Hoeller, Jia Lin Yuan, Ritvik Singh, Yunrong Guo, Hammad Mazhar, Ajay Mandlekar, Buck Babich, Gavriel State, Marco Hutter, and Animesh Garg. Orbit: A unified simulation framework for interactive robot learning environments. *IEEE Robotics and Automation Letters*, 8(6):3740–3747, 2023. doi: 10.1109/LRA.2023.3270034.

- Anusha Nagabandi, Gregory Kahn, Ronald S. Fearing, and Sergey Levine. Neural network dynamics for model-based deep reinforcement learning with model-free fine-tuning, 2017. URL <https://arxiv.org/abs/1708.02596>.
- David Rolnick, Arun Ahuja, Jonathan Schwarz, Timothy Lillicrap, and Gregory Wayne. Experience replay for continual learning. *Advances in neural information processing systems*, 32, 2019.
- Nikita Rudin, David Hoeller, Philipp Reist, and Marco Hutter. Learning to walk in minutes using massively parallel deep reinforcement learning, 2022. URL <https://arxiv.org/abs/2109.11978>.
- John Schulman, Filip Wolski, Prafulla Dhariwal, Alec Radford, and Oleg Klimov. Proximal policy optimization algorithms. *arXiv preprint arXiv:1707.06347*, 2017a.
- John Schulman, Filip Wolski, Prafulla Dhariwal, Alec Radford, and Oleg Klimov. Proximal policy optimization algorithms, 2017b. URL <https://arxiv.org/abs/1707.06347>.
- Haojie Shi and Max Q-H Meng. Deep koopman operator with control for nonlinear systems. *IEEE Robotics and Automation Letters*, 7(3):7700–7707, 2022.
- Lu Shi, Masih Haseli, Giorgos Mamakoukas, Daniel Bruder, Ian Abraham, Todd Murphey, Jorge Cortes, and Konstantinos Karydis. Koopman operators in robot learning, 2024. URL <https://arxiv.org/abs/2408.04200>.
- Lixing Song, Junheng Wang, and Junhong Xu. A data-efficient reinforcement learning method based on local koopman operators. In *2021 20th IEEE International Conference on Machine Learning and Applications (ICMLA)*, pages 515–520, 2021. doi: 10.1109/ICMLA52953.2021.00086.
- Masaki Murooka Sotaro Katayama and Yuichi Tazaki. Model predictive control of legged and humanoid robots: models and algorithms. *Advanced Robotics*, 37(5):298–315, 2023. doi: 10.1080/01691864.2023.2168134. URL <https://doi.org/10.1080/01691864.2023.2168134>.
- Joel A Tropp. User-friendly tail bounds for sums of random matrices. *Foundations of computational mathematics*, 12:389–434, 2012.
- Pierre-Brice Wieber, Russ Tedrake, and Scott Kuindersma. Modeling and control of legged robots. In *Springer Handbook of Robotics, 2nd Ed.*, 2016. URL <https://api.semanticscholar.org/CorpusID:6790710>.
- Matthew O. Williams, Ioannis G. Kevrekidis, and Clarence W. Rowley. A data-driven approximation of the koopman operator: Extending dynamic mode decomposition. *Journal of Nonlinear Science*, page 1307–1346, Dec 2015. doi: 10.1007/s00332-015-9258-5. URL <http://dx.doi.org/10.1007/s00332-015-9258-5>.
- Zeji Yi, Chaoyi Pan, Guanqi He, Guannan Qu, and Guanya Shi. Covo-mpc: Theoretical analysis of sampling-based mpc and optimal covariance design, 2024. URL <https://arxiv.org/abs/2401.07369>.

Peng Yin, Abulikemu Abuduweili, Shiqi Zhao, Lingyun Xu, Changliu Liu, and Sebastian Scherer. Bioslam: A bioinspired lifelong memory system for general place recognition. *IEEE Transactions on Robotics*, 2023.

Weiye Zhao, Feihan Li, Yifan Sun, Rui Chen, Tianhao Wei, and Changliu Liu. Absolute policy optimization: Enhancing lower probability bound of performance with high confidence. In *Forty-first International Conference on Machine Learning*.

James Zhu, J. Joe Payne, and Aaron M. Johnson. Convergent ilqr for safe trajectory planning and control of legged robots, 2024. URL <https://arxiv.org/abs/2304.00346>.

Appendix A. Related Works

Controlling Nonlinear Dynamics. Nonlinear dynamic systems are generally controlled using two main approaches: model-free and model-based methods. Model-free methods, often associated with learning-based approaches, have become popular for addressing complex, high-dimensional systems in a data-driven manner. Reinforcement learning (RL) techniques, for instance, approximate a combination of system dynamics and control policies by training neural networks using methods like policy gradients or value iteration. Off-policy algorithms such as SAC [Haarnoja et al. \(2018\)](#) efficiently reuse data to learn control policies, whereas on-policy methods like PPO [Schulman et al. \(2017a\)](#) and its extension APO [Zhao et al.](#) ensure monotonic policy improvement. Another learning paradigm, imitation learning [Luo et al. \(2023\)](#); [He et al. \(2024\)](#), leverages large expert datasets to guide policy development. Despite their successes, these methods often suffer from challenges such as sample inefficiency, high computational cost, and limited generalization.

Model-based methods, on the other hand, rely on leveraging system physics to construct accurate models. Techniques like iLQR [Li and Todorov \(2004\)](#) and NMPC [Grüne et al. \(2017\)](#); [Liu et al. \(2023\)](#) use these models to optimize control trajectories, while methods such as backstepping [Fossen and Grovlen \(1998\)](#) are well-suited for systems with well-defined dynamics. Neural network-based approaches, such as [Nagabandi et al. \(2017\)](#), extend these ideas by approximating nonlinear dynamics for control tasks. Moreover, model-based RL combines data-driven techniques with physical modeling to describe nonlinear system dynamics. For instance, [Song et al. \(2021\)](#) uses RL workflows to fit multiple local approximations of global dynamics, while [Nagabandi et al. \(2017\)](#) employs RL reward functions to learn dynamics from extensive random-shooting data. However, even these approaches face significant challenges when applied to high-dimensional systems, such as legged robots, where designing accurate models becomes increasingly complex and task-specific.

Koopman Operator Theory. While model-based methods struggle with complex, high-dimensional systems and model-free methods lack interpretability and flexibility, linearizing nonlinear dynamics has recently emerged as a promising approach. Among these, Koopman Operator Theory has garnered attention for its ability to represent nonlinear dynamics in a higher-dimensional linear space. Current research on Koopman theory in control can be categorized into three main directions:

(i) Koopman Operator as a Feature Encoder: The Koopman operator has been applied in some methods to predict future states based on the current state [Han et al. \(2023\)](#) or vision inputs [Chen et al. \(2024\)](#). However, these approaches primarily serve as feature extractors and do not fully exploit the benefits of linearization. Additionally, designing an effective Koopman operator is often challenging due to the requirement for infinite-dimensional representations and the inefficiency of available data [Kaiser et al. \(2020\)](#).

(ii) Integrating Koopman Operators with RL: Other methods combine the Koopman latent dynamic space with traditional RL policies, either hierarchically [Kim et al. \(2024a\)](#) or end-to-end [Lyu et al. \(2023\)](#). While this integration aims to benefit from Koopman’s properties, it still inherits the challenges of learning-based methods, particularly in terms of interpretability and generalization.

(iii) Linear Control in Koopman Latent Space: A promising direction applies traditional linear control methods, such as LQR or MPC, to the Koopman-linearized model, emphasizing interpretability and flexibility. For example, [Shi and Meng \(2022\)](#) applies LQR to a deep-learned Koopman operator, while others use radial basis functions (RBF) [Korda and Mezić \(2018b\)](#) or derivative basis functions [Mamakoukas et al. \(2021\)](#) to design the operator. Despite these advances, current methods

struggle to control high-dimensional systems, like legged robots due to severe model mismatch and domain shifts.

Finally, research has begun addressing the errors that arise during the Koopman dynamics learning process. Works such as [Kim et al. \(2024b\)](#) and [Korda and Mezić \(2018a\)](#) evaluate the reconstruction and projection errors, providing valuable theoretical foundations for further improvement.

Continual Learning. Continual learning is designed to incrementally update knowledge derived from streaming data. A prevalent approach in this field is memory replay [Rolnick et al. \(2019\)](#), where selected samples are stored and repeatedly replayed to train the model through methods such as random sampling [Rolnick et al. \(2019\)](#) or importance sampling [Yin et al. \(2023\)](#); [Abuduweili and Liu \(2023\)](#). Our method employs a random replay strategy. Another relevant approach is the use of dynamic architecture-based methods, exemplified by Learning without Forgetting (LwF) [Li and Hoiem \(2017\)](#) and PackNet [Mallya and Lazebnik \(2018\)](#), which modify the neural network architecture incrementally during training. Unlike these methods, which primarily add parameters to the final layers for incremental learning of classification tasks, our approach utilizes a theory-guided strategy to increase the latent state dimension, thereby enhancing the accuracy of the dynamics model.

Appendix B. Algorithm

Algorithm 1 presents the proposed algorithm for Incremental Learning using the Koopman Operator.

Appendix C. Additional Experiments

C.1. Computational Cost Comparison

We compare the resource usage of all algorithms in terms of GPU and CPU consumption, as well as wall-clock time, using DKUC as a benchmark, as presented in Figure 6. The horizontal axis in the upper area represents the percentage of resource usage relative to DKUC, while the horizontal axis in the lower area displays the running time (in seconds). The experiments are based on the averages from all seven test suites set for tracking experiments, as described in Section 4.3, and were run and averaged over three different seeds. Our algorithms utilize nearly the same GPU and CPU resources as the baseline methods while demonstrating a sharp lead in k-step prediction and tracking experiments. Furthermore, although wall-clock time increases when compared to DKUC and DKAC methods, it remains low enough to facilitate real-time inference for efficient control of real robots while NNDM method spends unacceptable reasoning time, demonstrating the effectiveness of the Koopman method and our algorithms, thereby addressing Q5.

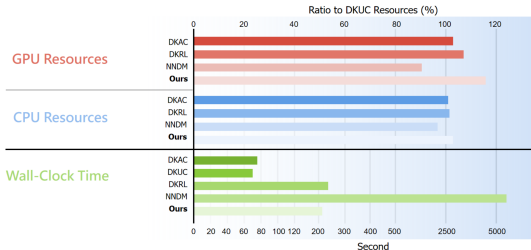


Figure 6: Computational cost(GPU occupancy, CPU occupancy and wall-clock time) comparison

Algorithm 1 Incremental Koopman Algorithm

Input: MPC Controller π_{mpc} , Initial latent space dimension $n^{(0)}$, Initial dynamics $\mathcal{T}^{(0)} = (g_{n^{(0)}}, A_{n^{(0)}}, B_{n^{(0)}})$, Initial dataset $\mathcal{D}^{(0)}$, Reference repository \mathcal{R} , Dimension increment step size Δn and Initial training epochs $J^{(0)}$

Function: TrainKoopman(n, \mathcal{D}, J):

$optimizer \leftarrow Adam()$;

$scheduler \leftarrow CosineAnnealingLR()$;

$\mathcal{T} \doteq (g_n, A_n, B_n)$; {Initialization of Koopman dynamics}

for $k = 0, 1, 2, \dots, J - 1$ **do**

for \mathcal{B} in \mathcal{D} **do**

$\mathcal{B}_z \leftarrow g(\mathcal{B})$; {Embed $x \in \mathcal{B}$ into latent vectors z }

$l_k \leftarrow \mathcal{L}_{koopman}(\mathcal{T}, \mathcal{B}, \mathcal{B}_z)$; {Refer to Equation (6) for $\mathcal{L}_{koopman}$ }

$optimizer.zero_grad()$;

$l_k.backward()$;

$optimizer.step()$;

end for

$scheduler.step()$;

end for

$return \mathcal{T}$;

for $j = 0, 1, 2, \dots$ **do**

$n^{(j+1)} \leftarrow n^{(j)} + \Delta n$; {Increase latent space dimension}

$\mathcal{D}_{incre}^{(j+1)} \leftarrow \pi_{mpc}(\mathcal{T}^{(j)}, \mathcal{R})$;

$\mathcal{D}^{(j+1)} \leftarrow \{\mathcal{D}^{(j)}, \mathcal{D}_{incre}^{(j+1)}\}$; {Dataset augmentation}

$J^{(j+1)} \leftarrow J^{(j)}$;

$\mathcal{T}^{(j+1)} \leftarrow \text{TrainKoopman}(n^{(j+1)}, \mathcal{D}^{(j+1)}, J^{(j+1)})$;

while TrainKoopman failed **do**

$J^{(j+1)} \leftarrow \frac{J^{(j+1)}}{2}$; {Adjust epochs when collapsing}

$\mathcal{T}^{(j+1)} \leftarrow \text{TrainKoopman}(n^{(j+1)}, \mathcal{D}^{(j+1)}, J^{(j+1)})$;

end while

if TrackConverge($\mathcal{T}^{(j+1)}, \mathcal{T}^{(j)}$) **then**

 Break; {Quit if tracking performance converge}

end if

end for

C.2. Evaluation of the theorem

We conducted experiments on the G1 robot to evaluate the conclusions of Theorem 1 and Theorem A.3. Figure Figure 7(a) illustrates the prediction error versus sample size with a fixed embedding dimension of $n = 500$. Consistently, the prediction error decreases as the sample size increases, aligning with the decreasing rate outlined in Equation (33). Figure Figure 7(b) displays the prediction error versus embedding dimension (or Koopman dimension) for a fixed sample size of $m = 180,000$. Similarly, an increase in the embedding dimension results in a decrease in prediction error, echoing the trend described in Equation (49).

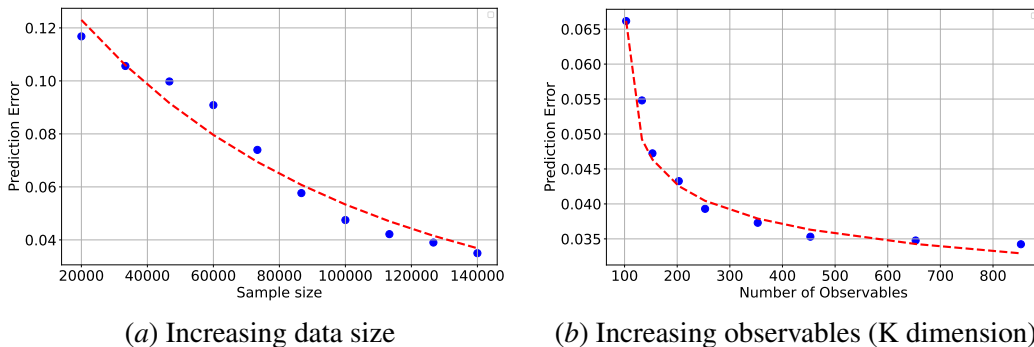


Figure 7: Validation of theorem 1.

Appendix D. Proof of Koopman operator convergence

In this section, we discuss the theoretical properties of the proposed algorithm. The convergence of data-driven Koopman operator algorithms, particularly the Extended Dynamic Mode Decomposition (EDMD) Williams et al. (2015), has been rigorously established in prior works Korda and Mezić (2018a,b). Specifically, Korda and Mezić Korda and Mezić (2018a) demonstrate that, under mild assumptions, as the sample size $m \rightarrow \infty$ and the dimension of latent state (or also called number of observables) $n \rightarrow \infty$, the estimated Koopman operator \hat{K} converges to the true Koopman operator \mathcal{K} . Our theoretical analysis builds upon the results presented in Korda and Mezić (2018a,b) but differs by providing explicit convergence rates under additional assumptions. In the following sections, we focus primarily on autonomous systems without control inputs. For control systems, the results can be extended by setting $s = [x; u]^\top$.

D.1. Preliminary

Koopman Operator Theory. For clarity, we adopt terminology slightly different from that used in the main content. Here s^+ denotes the next state of s . Consider a dynamical system $s^+ = f(s)$, with $f : \mathcal{S} \rightarrow \mathcal{S}$, where \mathcal{S} is a given separable topological space. Let \mathcal{H} represent a separable Hilbert space, equipped with an inner product $\langle \cdot, \cdot \rangle$ and corresponding norm $\| \cdot \|$. The Koopman operator $\mathcal{K} : \mathcal{H} \rightarrow \mathcal{H}$ is defined as $\mathcal{K}\phi = \phi \circ f$, where $\phi \in \mathcal{H}$ are embedding functions.

Extended Dynamic Mode Decomposition (EDMD). EDMD is a data-driven method for approximating the Koopman operator \mathcal{K} within a finite-dimensional subspace. Our methodology aligns with the EDMD approach. Given an embedding function (observable) $\Phi(s) = [\phi_1(s), \phi_2(s), \dots, \phi_n(s)]^\top$, where $\phi_i : \mathcal{S} \rightarrow \mathbb{R}$ for $i \in [1, n]$. Given m data pairs $\{(s_i, s_i^+)\}_{i=1}^m$, EDMD seeks a finite-dimensional

Koopman matrix $K_{n,m} \in \mathbb{R}^{n \times n}$ that best fits the data according to the following optimization problem:

$$\min_{K \in \mathbb{R}^{n \times n}} \sum_{i=1}^m \|\Phi(s_i^+) - K\Phi(s_i)\|_2^2 \quad (9)$$

Assuming that the Gram matrix $G_{n,m}$ is invertible, the closed-form solution for the Koopman matrix is derived from:

$$K_{n,m} = A_{n,m}G_{n,m}^{-1} \quad (10)$$

$$G_{n,m} = \frac{1}{m} \sum_{i=1}^m \Phi(s_i)\Phi(s_i)^\top, \quad A_{n,m} = \frac{1}{m} \sum_{i=1}^m \Phi(s_i)\Phi(s_i^+)^\top \quad (11)$$

Denoting \mathcal{H}_n the span of $\phi_1(s), \phi_2(s), \dots, \phi_n(s)$. It is notable that any function $g \in \mathcal{H}_n$ can be represented as $g = c^\top \Phi$, where $c \in \mathbb{R}^n$.

EDMD as L_2 projection. As shown by [Korda and Mezić \(2018a\)](#), EDMD approximates the finite-dimensional Koopman operator through an L_2 projection of the true Koopman operator. We interpret these results as follows. Consider an arbitrary nonnegative measure μ on the state space \mathcal{S} , and let $L_2(\mu)$ denote the Hilbert space of all square integrable functions with respect to the measure μ . We define the $L_2(\mu)$ projection, denoted as \mathcal{P}_n^μ , of a function g onto \mathcal{H}_n :

$$\mathcal{P}_n^\mu g = \arg \min_{h \in \mathcal{H}_n} \|h - g\|_{L_2(\mu)} = \arg \min_{h \in \mathcal{H}_n} \int_{\mathcal{S}} (h - g)^2 d\mu = \Phi^\top \arg \min_{c \in \mathbb{R}^n} \int_{\mathcal{S}} (c^\top \Phi - g)^2 d\mu. \quad (12)$$

We now state a key property of $K_{n,m}$ as follows.

Theorem A.1 [Korda and Mezić \(2018a\)](#). Let $\hat{\mu}_m$ denote the empirical measure associated to the points s_1, \dots, s_m , i.e., $\hat{\mu}_m = \frac{1}{m} \sum_{i=1}^m \delta_{s_i}$, where δ_{s_i} denotes the Dirac measure at s_i . Then for any $g \in \mathcal{H}_n$,

$$K_{n,m}g = \mathcal{P}_n^{\hat{\mu}_m} \mathcal{K}g = \arg \min_{h \in \mathcal{H}_n} \|h - \mathcal{K}g\|_{L_2(\hat{\mu}_m)}, \quad \text{i.e. } K_{n,m} = \mathcal{P}_n^{\hat{\mu}_m} \mathcal{K}|_{\mathcal{H}_n}, \quad (13)$$

where $\mathcal{K}|_{\mathcal{H}_n} : \mathcal{H}_n \rightarrow \mathcal{H}$ is the restriction of the Koopman operator to the subspace \mathcal{H}_n .

The theorem states that the estimated Koopman operator $K_{n,m}$ is the L_2 projection of the true Koopman operator \mathcal{K} on the span of ϕ_1, \dots, ϕ_n with respect to the empirical measure on the samples s_1, \dots, s_m .

Consequently, the total error in approximating the true Koopman operator \mathcal{K} with its learned finite-dimensional estimate $K_{n,m}$ can be decomposed into two components: projection error and sampling error. *Sampling error:* The sampling error, denoted as $\epsilon_{\text{samp}}(n, m) = \|K_{n,m} - K_n\|$, originates from estimating the finite-dimensional Koopman operator K_n using a finite number of data samples m . *Projection error:* The projection error, denoted as $\epsilon_{\text{proj}}(n) = \|K_n \mathcal{P}_n^\mu - \mathcal{K}\|$, arises from the approximation of the infinite-dimensional Koopman operator \mathcal{K} within a finite-dimensional subspace. This conceptual framework forms the basis for the overall proof scheme presented in prior work by Korda and Mezić [Korda and Mezić \(2018a\)](#). In contrast, we extend these results by providing explicit convergence rates under certain additional assumptions.

D.2. Convergence of Sampling error

We begin by establishing the assumptions necessary for our analysis.

Assumption 1 (i.i.d samples). Data samples s_1, \dots, s_m are drawn independently from the distribution μ .

Assumption 2 (Bounded latent state). The norm of the latent state vector is bounded. Specifically, there exists a constant $B > 0$ such that $\|\Phi(s)\| \leq B$ for all $s \in \mathcal{S}$.

Assumption 3 (Invertible Gram matrix). The Gram matrix $G_{n,m}$ defined in eq. (11) is invertible, and its smallest eigenvalue is bounded below by $\gamma > 0$, such as $\lambda_{\min}(G_{n,m}) \geq \gamma$.

Assumption 1 ensures the independence of samples, which can be relaxed if the dynamical system f is ergodic and the samples s_1, \dots, s_m are taken along a trajectory of the system starting from some initial condition $s_0 \in \mathcal{S}$. Assumption 2 can be satisfied in neural network implementations by using bounded activation functions (e.g., sigmoid functions) or by constraining the network weights. While Assumption 3 requires the Gram matrix to be invertible with a bounded eigenvalue, this condition can be relaxed in practice by employing the pseudoinverse of the Gram matrix.

Under Assumption 3, the learned Koopman operator $K_{n,m}$ can be computed using eq. (10). We consider the sampling error between the learned Koopman operator $K_{n,m}$ with finite data size m , and the Koopman operator K_n obtained as the L_2 projection of the true Koopman operator onto the subspace \mathcal{H}_n with infinite data:

$$\epsilon_{\text{samp}}(n, m) = \|K_{n,m} - K_n\| = \|G_{n,m}^{-1}A_{n,m} - G_n^{-1}A_n\| \quad (14)$$

Here, $G_{n,m}$ and $A_{n,m}$ are computed using finite samples via eq. (11). While G_n and A_n represent their expected values, equivalent to computing eq. (11) with an infinite number of samples. Under Assumption 1, by the Law of Large Numbers, $G_{n,m}$ and $A_{n,m}$ converge to the expected value G_n and A_n respectively as $m \rightarrow \infty$. Then we have:

$$G_n = \mathbb{E}[G_{n,m}] = \mathbb{E}\left[\frac{1}{m} \sum_{i=1}^m \Phi(s_i)\Phi(s_i)^\top\right], \quad A_n = \mathbb{E}[A_{n,m}] = \mathbb{E}\left[\frac{1}{m} \sum_{i=1}^m \Phi(s_i)\Phi(s_i^+)^\top\right] \quad (15)$$

We proceed to decompose the sampling error:

$$\begin{aligned} \epsilon_{\text{samp}}(n, m) &= \|A_{n,m}G_{n,m}^{-1} - A_nG_n^{-1}\| = \|A_{n,m}G_{n,m}^{-1} - A_{n,m}G_n^{-1} + A_{n,m}G_n^{-1} - A_nG_n^{-1}\| \\ &\leq \|A_{n,m}\| \cdot \|G_{n,m}^{-1} - G_n^{-1}\| + \|A_{n,m} - A_n\| \cdot \|G_n^{-1}\|. \end{aligned} \quad (16)$$

To bound each term in eq. (16), we utilize properties of matrix norms and inequalities. First, we consider the difference of the inverses of $G_{n,m}$ and G_n . Using the identity $G_{n,m}^{-1} - G_n^{-1} = G_n^{-1}(G_n - G_{n,m})G_{n,m}^{-1}$, we have:

$$\|G_{n,m}^{-1} - G_n^{-1}\| \leq \|G_n^{-1}\| \|G_n - G_{n,m}\| \|G_{n,m}^{-1}\|. \quad (17)$$

Based on the assumption 2, the spectral norm of $A_{m,n}$ can be bounded:

$$\|A_{n,m}\| \leq \frac{1}{m} \sum_{t=1}^m \|\Phi(s_t)\| \|\Phi(s_t^+)\| \leq B^2 \quad (18)$$

Similarly, under Assumption 3, the norms of inverse gram matrices are bounded

$$\|G_{n,m}^{-1}\| = \frac{1}{\lambda_{\min}(G_{n,m})} \leq \frac{1}{\gamma}, \quad \|G_n^{-1}\| \leq \frac{1}{\gamma} \quad (19)$$

Substituting eqs. (17) to (19) back to eq. (16), we obtain:

$$\epsilon_{\text{samp}}(n, m) \leq \frac{B^2}{\gamma^2} \|G_{n,m} - G_n\| + \frac{1}{\gamma} \|A_{n,m} - A_n\| \quad (20)$$

To bound $\|G_{n,m} - G_n\|$ and $\|A_{n,m} - A_n\|$, we utilize the Matrix Bernstein Inequality [Tropp \(2012\)](#), which provides concentration bounds for sums of independent random matrices.

Matrix Bernstein Inequality. Let $\{Y_i\}_{i=1}^m$ be independent, mean-zero random matrices with dimensions $d_1 \times d_2$. Assume that each matrix satisfies $\|Y_i\| \leq L$ almost surely. Define the variance parameter

$$\sigma^2 = \left\| \sum_{i=1}^m \mathbb{E}[Y_i Y_i^\top] \right\|. \quad (21)$$

Then, for all $\epsilon \geq 0$,

$$\mathbb{P} \left(\left\| \sum_{i=1}^m Y_i \right\| \geq \epsilon \right) \leq (d_1 + d_2) \exp \left(\frac{-\epsilon^2/2}{\sigma^2 + L\epsilon/3} \right). \quad (22)$$

We apply the Matrix Bernstein Inequality to bound $\|A_{n,m} - A_n\|$. Define Y_i as:

$$Y_i = \frac{1}{m} \left(\Phi(s_i) \Phi(s_i^+)^\top - \mathbb{E}[\Phi(s_i) \Phi(s_i^+)^\top] \right). \quad (23)$$

Then $A_{n,m} - A_n = \sum_{i=1}^m Y_i$, and $E[Y_i] = 0$. Under Assumption 2, the norm of Y_i is bounded:

$$\|Y_i\| \leq \frac{2}{m} \cdot \|\Phi(s_i)\| \cdot \|\Phi(s_i^+)\| \leq \frac{2B^2}{m} \quad (24)$$

the variance parameter σ^2 is bounded as follows:

$$\sigma^2 = \left\| \sum_{i=1}^m \mathbb{E}[Y_i Y_i^\top] \right\| \leq \sum_{i=1}^m \|\mathbb{E}[Y_i Y_i^\top]\| \leq \sum_{i=1}^m \left(\frac{2B^2}{m} \right)^2 = \frac{4B^4}{m} \quad (25)$$

Applying the Matrix Bernstein Inequality with $d_1 = d_2 = n$, $L = \frac{2B^2}{m}$, $\sigma^2 = \frac{4B^4}{m}$, we obtain:

$$\mathbb{P} (\|A_{n,m} - A_n\| \geq \epsilon) = \mathbb{P} \left(\left\| \sum_{i=1}^m Y_i \right\| \geq \epsilon \right) \leq 2n \exp \left(\frac{-\epsilon^2 m/2}{4B^4 + \frac{2B^2 \epsilon}{3}} \right). \quad (26)$$

Assuming $\epsilon < B^2$, and for sufficiently large m , the term $4B^4$ dominates $\frac{2B^2 \epsilon}{3}$, allowing us to simplify the bound:

$$\mathbb{P} (\|A_{n,m} - A_n\| \geq \epsilon) \leq 2n \exp \left(-\frac{m\epsilon^2}{8B^4} \right). \quad (27)$$

This bound holds in probability. To ensure that the probability is at most δ , we set:

$$2n \exp\left(-\frac{m\epsilon^2}{8B^4}\right) \leq \delta. \quad (28)$$

Solving for ϵ , we find:

$$\epsilon \geq \sqrt{\frac{8B^4 \ln(2n/\delta)}{m}}. \quad (29)$$

Thus, with probability at least $1 - \delta$, the following inequality holds,

$$\|A_{n,m} - A_n\| \leq \sqrt{\frac{8B^4 \ln(2n/\delta)}{m}}. \quad (30)$$

A similar procedure applies to bound $\|G_{n,m} - G_n\|$. Using the Matrix Bernstein Inequality with probability at least $1 - \delta$,

$$\|G_{n,m} - G_n\| \leq \sqrt{\frac{8B^4 \ln(2n/\delta)}{m}}. \quad (31)$$

Substituting eqs. (30) and (31) into eq. (20), we obtain, with probability at least $(1 - \delta)^2$,

$$\epsilon_{\text{samp}}(n, m) \leq \frac{B^2}{\gamma^2} \sqrt{\frac{8B^4 \ln(2n/\delta)}{m}} + \frac{1}{\gamma} \sqrt{\frac{8B^4 \ln(2n/\delta)}{m}} = \frac{2B^2 \sqrt{2 \ln(2n/\delta)}}{\gamma \sqrt{m}} \left(\frac{B^2}{\gamma} + 1 \right) \quad (32)$$

For simplicity, we mainly consider the convergence rate related to m, n , and then with a high probability,

$$\epsilon_{\text{samp}}(n, m) \leq \mathcal{O}\left(\sqrt{\frac{\ln(n)}{m}}\right) \quad (33)$$

For larger sample sizes m , such that $m = \mathcal{O}(n \ln(n))$, with high probability we have:

$$\epsilon_{\text{samp}}(n, m)|_{m=\mathcal{O}(n \ln(n))} \leq \mathcal{O}\left(\frac{1}{\sqrt{n}}\right) \quad (34)$$

This result indicates that, under the given assumptions, the sampling error decreases inversely with the square root of the number of observables n , when the number of samples m grows proportionally to $n \ln n$.

D.3. Convergence of Projection Error

In this section, we establish the convergence of the projection error $\epsilon_{\text{proj}}(n)$ as the dimension n of the subspace \mathcal{H}_n increases. We begin by introducing additional assumptions necessary for our analysis.

Assumption 4 (Orthogonal basis). *The embedding functions ϕ_1, \dots, ϕ_n are orthogonal (independent). i.e. $\langle \phi_i, \phi_j \rangle = \delta_{ij}$, for all $i, j = 1, \dots, n$, where δ_{ij} is the Kronecker delta.*

Assumption 5 (Bounded Koopman Operator). *The Koopman operator $\mathcal{K} : \mathcal{H} \rightarrow \mathcal{H}$ is bounded, i.e. $\|\mathcal{K}\| \leq M < \infty$.*

Assumption 4 is nonrestrictive since any countable dense subset of \mathcal{H} can be orthonormalized using the Gram–Schmidt process. Assumption 5 holds, for instance, when the system dynamics are Lipschitz continuous and the state space is bounded.

Given a function $\psi \in \mathcal{H}$, we define the projection error as

$$\epsilon_{\text{proj}}(n) = \|K_n \mathcal{P}_n^\mu \psi - \mathcal{K}\psi\| = \int_{\mathcal{S}} \|K_n \mathcal{P}_n^\mu \psi - \mathcal{K}\psi\| d\mu \quad (35)$$

where K_n is the finite-dimensional approximation of the Koopman operator defined on \mathcal{H}_n , and \mathcal{P}_n^μ is the orthogonal projection onto \mathcal{H}_n .

We decompose ψ into its projection onto \mathcal{H}_n and its orthogonal complement: $\psi = \mathcal{P}_n^\mu \psi + (I - \mathcal{P}_n^\mu)\psi$, where I is the identity operator. Then we have:

$$\epsilon_{\text{proj}}(n) = \|K_n \mathcal{P}_n^\mu \psi - \mathcal{K}\psi\| \quad (36)$$

$$= \|K_n \mathcal{P}_n^\mu \mathcal{P}_n^\mu \psi - \mathcal{K} \mathcal{P}_n^\mu \psi + K_n \mathcal{P}_n^\mu (I - \mathcal{P}_n^\mu)\psi - \mathcal{K}(I - \mathcal{P}_n^\mu)\psi\| \quad (37)$$

According to the definition of the orthogonal projection \mathcal{P}_n^μ , we have $\mathcal{P}_n^\mu \mathcal{P}_n^\mu \psi = \mathcal{P}_n^\mu \psi$, $\mathcal{P}_n^\mu \cdot (I - \mathcal{P}_n^\mu)\psi = 0$. Recall from Theorem A.1 that $K_n = \mathcal{P}_n^\mu \mathcal{K}$. Therefore, we can rewrite eq. (37) as :

$$\epsilon_{\text{proj}}(n) = \|K_n \mathcal{P}_n^\mu \psi - \mathcal{K} \mathcal{P}_n^\mu \psi - \mathcal{K}(I - \mathcal{P}_n^\mu)\psi\| \quad (38)$$

$$= \|(\mathcal{P}_n^\mu - I)\mathcal{K} \mathcal{P}_n^\mu \psi + \mathcal{K}(\mathcal{P}_n^\mu - I)\psi\| \quad (39)$$

$$\leq \|(\mathcal{P}_n^\mu - I)\| \|\mathcal{K} \mathcal{P}_n^\mu \psi\| + \|\mathcal{K}\| \|(\mathcal{P}_n^\mu - I)\| \|\psi\| \quad (40)$$

Under Assumption 5, $\|\mathcal{K}\| \leq M$. Under assumption 2, $\|\phi_i\| \leq B$. Let $\psi = \sum_{i=1}^{\infty} c_i \phi_i$. By Parseval's identity $\sum_{i=1}^{\infty} |c_i|^2 = 1$. Then $\|\psi\| \leq B$. Therefore, we can rewrite eq. (40) as :

$$\epsilon_{\text{proj}}(n) \leq 2MB \|(\mathcal{P}_n^\mu - I)\| \quad (41)$$

From Equation (41), we observe that the projection error depends on the norm of the residual $(\mathcal{P}_n^\mu - I)\psi$. As $n \rightarrow \infty$, the subspace \mathcal{H}_n becomes dense in \mathcal{H} , and \mathcal{P}_n^μ converges strongly to the identity operator I [Korda and Mezić \(2018a\)](#). Therefore,

$$\lim_{n \rightarrow \infty} \epsilon_{\text{proj}}(n) = 0, \quad \lim_{n \rightarrow \infty} K_n \mathcal{P}_n^\mu = \mathcal{K} \quad (42)$$

Recall that K_n is an operator on the finite-dimensional subspace \mathcal{H}_n spanned by the embedding functions ϕ_1, \dots, ϕ_n . And \mathcal{K} is an operator on \mathcal{H} . The convergence of K_n to \mathcal{K} implies convergence of their eigenvalues and eigenfunctions under certain conditions. Prior work [Korda and Mezić \(2018a\)](#) shows the convergence of eigenvalue as the following theorem.

Theorem A.2 [Korda and Mezić \(2018a\)](#). *If assumption 4 and assumption 5 holdes, and λ_n is a sequeance of eigenvalue of K_n with associated normalized eigenfunctions $\phi_n \in \mathcal{H}_n$, then there exists a subsequence $(\lambda_{n_i}, \phi_{n_i})$ such that*

$$\lim_{i \rightarrow \infty} \lambda_{n_i} = \lambda^*, \quad \phi_{n_i} \xrightarrow{\text{weak convergence}} \phi^* \quad (43)$$

where $\lambda^* \in \mathbb{C}$ and $\phi^* \in \mathcal{H}$ are eigenvalue and eigenfunction of Koopman operator, such that $\mathcal{K}\phi^* = \lambda^* \phi^*$.

This theorem demonstrates the convergence of eigenvalues and eigenfunctions of K_n to those of \mathcal{K} as $n \rightarrow \infty$. Let the sorted (decreasing order) eigenvalues of the Koopman operator \mathcal{K} are $\lambda_1^*, \lambda_2^*, \dots$, and corresponding eigenfunctions are $\phi_1^*, \phi_2^*, \dots$. The sorted eigenvalues of the K_n are $\lambda_1, \lambda_2, \dots, \lambda_n$, and corresponding eigenfunctions are $\phi_1, \phi_2, \dots, \phi_n$. To provide an explicit convergence rate for the projection error, we introduce further assumptions.

Assumption 6 (Spectral Properties of \mathcal{K}). *The eigenvalues of the Koopman operator \mathcal{K} decay sufficiently fast, for instance, $|\lambda_i| \leq \frac{C}{i^\alpha}$ for some constant $C > 0, \alpha > \frac{1}{2}$.*

Assumption 7 (Properly learned eigenfunctions). *The embedding functions $\Phi(\cdot) = [\phi_1, \dots, \phi_n]^\top$ correspond to the first n eigenfunctions of \mathcal{K} associated with the largest eigenvalues in magnitude. That is, $\lambda_i = \lambda_i^*$ or $\langle \lambda_i \phi_i, f \rangle = \langle \lambda_i^* \phi_i^*, \mathcal{P}_n^\mu f \rangle$ for $f \in \mathcal{H}$.*

Assumption 6 holds for systems where the Koopman operator has rapidly decaying spectral components, such as stable linear systems. Assumption 7 implies that the learned embedding functions capture the most significant modes of the system, which is reasonable given the universal approximation capabilities of neural networks and the optimization objective in Equation (9).

Under assumption 7, we can quantify the convergence rate of $\epsilon_{\text{proj}}(n)$. Let $\psi \in \mathcal{H}$, be expressed in terms of the eigenfunctions of \mathcal{K} : $\psi = \sum_{i=1}^{\infty} c_i \phi_i^* \in \mathcal{H}$ with $\sum_{i=1}^{\infty} |c_i|^2 = 1$. The projection error is given by

$$\epsilon_{\text{proj}}(n) = \|K_n \mathcal{P}_n^\mu \psi - \mathcal{K} \psi\| = \left\| \sum_{i=1}^{\infty} c_i K_n \mathcal{P}_n^\mu \phi_i^* - \sum_{i=1}^{\infty} c_i \mathcal{K} \phi_i^* \right\| \quad (44)$$

$$= \left\| \sum_{i=1}^n c_i \lambda_i \phi_i^* - \sum_{i=1}^{\infty} c_i \lambda_i^* \phi_i^* \right\| = \left\| \sum_{i=1}^n c_i (\lambda_i - \lambda_i^*) \phi_i^* + \sum_{i=n+1}^{\infty} c_i \lambda_i^* \phi_i^* \right\| \quad (45)$$

$$= \left\| \sum_{i=n+1}^{\infty} c_i \lambda_i^* \phi_i^* \right\| \leq B \cdot \left(\sum_{i=n+1}^{\infty} |\lambda_i^*|^2 \right)^{1/2} \quad (46)$$

Considering assumption 6, we can estimate the projection error

$$\epsilon_{\text{proj}}(n) \leq B \left(\sum_{i=n+1}^{\infty} \left(\frac{C}{i^\alpha} \right)^2 \right)^{1/2} \leq BC \left(\int_n^{\infty} \frac{dx}{x^{2\alpha}} \right)^{1/2} \quad (47)$$

$$= BC \left(\frac{1}{(2\alpha - 1)n^{2\alpha-1}} \right)^{1/2} = \frac{BC}{\sqrt{2\alpha - 1}} \cdot \frac{1}{n^{\alpha - \frac{1}{2}}}. \quad (48)$$

Therefore, we have the convergence rate of projection error:

$$\epsilon_{\text{proj}}(n) \leq \mathcal{O} \left(\frac{1}{n^{\alpha - \frac{1}{2}}} \right) \quad (49)$$

For $\alpha = 1$, we have:

$$\epsilon_{\text{proj}}(n) \leq \mathcal{O} \left(\frac{1}{\sqrt{n}} \right) \quad (50)$$

Thus, under the given assumptions, the projection error decreases inversely with the square root of n .

D.4. Convergence of Koopman Operator Under Incremental Strategy

By combining the convergence results of the sampling error eq. (34) and the projection error eq. (42), we conclude that the estimated Koopman operator $K_{m,n}$ converges to the true Koopman operator \mathcal{K} . This convergence has also been established in previous work by Korda and Mezić [Korda and Mezić \(2018a\)](#).

Theorem A.3 *Under the assumptions of 1) data samples s_1, \dots, s_m are i.i.d distributed; 2) the latent state is bounded, $\|\phi(s)\| < \infty$; 3) the embedding functions ϕ_1, \dots, ϕ_n are orthogonal (independent). The learned Koopman operator $K_{m,n}$ converges to true Koopman Operator:*

$$\lim_{m=\Omega(n \ln(n)), n \rightarrow \infty} K_{m,n} \rightarrow \mathcal{K} \quad (51)$$

Unlike prior work, we provide explicit convergence rates for both the sampling error and the projection error eqs. (34) and (49), leading to an overall error bound for $K_{m,n}$.

Theorem A.4 *Under the assumptions of 1) data samples s_1, \dots, s_m are i.i.d distributed; 2) the latent state is bounded, $\|\phi(s)\| < \infty$; 3) the embedding functions ϕ_1, \dots, ϕ_n are orthogonal (independent).*

(a) **Sampling Error Rate:** *The sampling error decreases with the number of samples m as:*

$$\epsilon_{\text{samp}}(n, m) \leq \mathcal{O}\left(\sqrt{\frac{\ln(n)}{m}}\right) \quad (52)$$

(b) **Projection Error Rate:** *Assuming additional conditions: 4) The eigenvalues of the Koopman operator \mathcal{K} decay sufficiently fast, for instance, $|\lambda_i| \leq \frac{C}{i^\alpha}$ for some constant $C > 0, \alpha > \frac{1}{2}$. 5) The embedding functions $\Phi(\cdot) = [\phi_1, \dots, \phi_n]^\top$ correspond to the first n eigenfunctions of \mathcal{K} associated with the largest eigenvalues in magnitude. Then, the projection error decreases with n :*

$$\epsilon_{\text{proj}}(n) \leq \mathcal{O}\left(\frac{1}{n^{\alpha-\frac{1}{2}}}\right) \quad (53)$$

(c) **Overall Error Bound:** *The total approximation error between $K_{m,n}$ and true koopman operator \mathcal{K} satisfies:*

$$\text{error} \leq \mathcal{O}\left(\sqrt{\frac{\ln(n)}{m}}\right) + \mathcal{O}\left(\frac{1}{n^{\alpha-\frac{1}{2}}}\right) \quad (54)$$

We conducted experiments to evaluate the validity of Theorem A.4; the results are presented in Appendix [C.2](#).

Appendix E. Experiment Details

E.1. Task Settings

We summarize our test suites in Table [3](#), and present the tracking failure threshold ϵ_{fail} in Table [4](#). It is worth noting that robots performing different tasks have distinct physical structures and movement patterns, necessitating different ϵ_{fail} values. These hyperparameters are selected when the robot is on the verge of falling and entering an unrecoverable state.

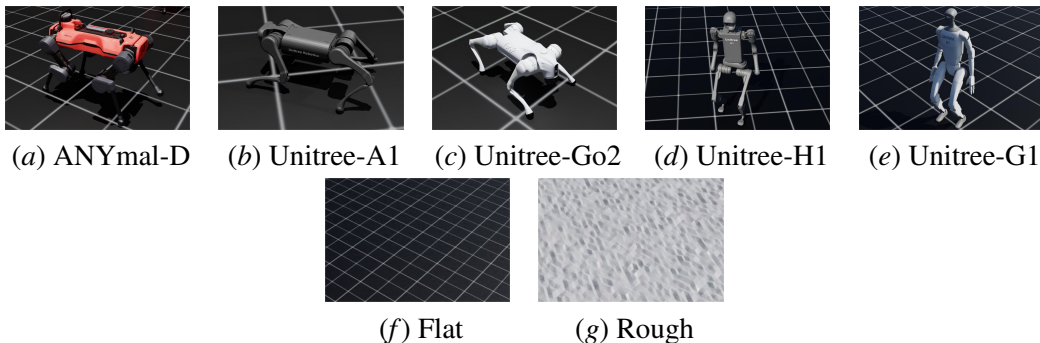


Figure 8: Legged robots and terrain in our test suites.

Table 3: The settings of test suites environment for our experiments

Task Settings		Producer		Terrain		Robot Type	
		Unitree	ANYmal	Flat	Rough	Quadruped	Humanoid
IsaacLab	Anyal-D (\mathbb{R}^{12})		✓	✓		✓	
	A1 (\mathbb{R}^{12})	✓		✓		✓	
	Go2 (\mathbb{R}^{12})	✓		✓	✓	✓	
Robot	H1 (\mathbb{R}^{19})	✓		✓			✓
	G1 (\mathbb{R}^{23})	✓		✓	✓		✓

E.2. Dataset Settings

All five legged robots are trained on IsaacLab [Mittal et al. \(2023\)](#). The initial dataset $\mathcal{D}^{(0)}$ consists of $6e4$ trajectories of length $l_{\mathcal{D}^{(0)}}$, and the reference repository \mathcal{R} , containing $3e3$ demonstrations of length $l_{\mathcal{R}}$ showcasing diverse and rich walking styles.

To achieve a more uniform data distribution under specific gait and contact modes, we apply random initialization techniques for constructing $\mathcal{D}^{(0)}$ and \mathcal{R} . First, we randomize the initial movement commands, including heading direction, x-axis linear velocity, and y-axis linear velocity in world coordinates, where the x-axis aligns with the heading direction and the y-axis is perpendicular to it. After collecting $6e4$ trajectories of length l_{init} (where $l_{init} > l_{\mathcal{D}^{(0)}}$), we randomly extract continuous segments of length $l_{\mathcal{D}^{(0)}}$ to enrich the robot’s range of motion and postures. All detailed hyperparameters are provided in Table 5.

In the following lifting phase, incremental dataset \mathcal{D}_{incre} , containing $3e4$ trajectories of length $l_{\mathcal{D}^{(0)}}$, will be added to the training dataset.

E.3. Algorithm Settings

The detailed dimensional information for the original and latent spaces for each task and algorithm is provided in Table 5. For simplicity, we organize the hyperparameters corresponding to each task in an array format as follows: (Flat-Anyal-D, Flat-Unitree-A1, Flat-Unitree-Go2, Rough-Unitree-Go2, Flat-Unitree-H1, Flat-Unitree-G1, Rough-Unitree-G1).

Table 4: The settings of hyperparameter ϵ_{fail} for test suites

ϵ_{fail} Settings		Anymal-D	A1	Go2	H1	G1
Terrain	Flat	0.18	0.16	0.16	0.15	0.10
Type	Rough	-	-	0.12	-	0.08

We set a fixed step size Δn for dimension increment at 100. The horizon length H for loss computation and MPC solving is set to 24 for the Unitree-H1 robot and 16 for the others.

All networks implemented for testing the algorithms are Residual Neural Networks (He et al. (2015)), featuring residual blocks structured as $\{\text{Linear}\}-\{\text{Relu}\}-\{\text{Linear}\}-\{\text{Residual}\}-\{\text{ReLU}\}$. The hidden dimensions and number of blocks are listed in Table 5. All networks are trained using the Adam optimizer with a Cosine Annealing learning rate scheduler. The initial learning rate and training epochs are 1e-3 and 100, respectively.

We normalize data in all test suites to mitigate the misaligned scale for each physical variable. The initial trajectories $m_{\mathcal{D}(0)}$ is set to 6e6 with initial trajectories length $l_{\mathcal{D}(0)}$ 100 for flat terrain and 200 for rough terrain. The clipped trajectory length l_{init} is equal with horizon length H . Then we construct reference repository \mathcal{R} with reference number $m_{\mathcal{R}}$ 3000 and reference length 500.

Other unique hyperparameters for each algorithm follow the original paper to attain best performance.

Each model is trained on a server with a 48-core Intel(R) Xeon(R) Silver 6426Y CPU @ 2.5.GHz, four Nvidia RTX A6000 GPU with 48GB memory, and Ubuntu 22.04.

E.4. Definition of Tracking Metrics

- Joint-relative mean per-joint position error (E_{JrPE}): $\frac{1}{200 * J} \sum_{t=1}^{200} \|j_t - j_t^*\|_1$, where j_t is the measured DoF position, j_t^* is the reference DoF position, J is the number of DoF.
- Joint-relative mean per-joint velocity error (E_{JrVE}): $\frac{1}{200 * J} \sum_{t=1}^{200} \|\dot{j}_t - \dot{j}_t^*\|_1$
- Joint-relative mean per-joint acceleration error (E_{JrAE}): $\frac{1}{200 * J} \sum_{t=1}^{200} \|\ddot{j}_t - \ddot{j}_t^*\|_1$
- Root mean position error (E_{RPE}): $\frac{1}{200 * 3} \sum_{t=1}^{200} \|p_t - p_t^*\|_1$, where p_t is the measured root position, p_t^* is the reference root position.
- Root mean linear velocity error (E_{RLVE}): $\frac{1}{200 * 3} \sum_{t=1}^{200} \|\dot{p}_t - \dot{p}_t^*\|_1$
- Root mean orientation error (E_{ROE}): $\frac{1}{200 * 4} \sum_{t=1}^{200} \|r_t - r_t^*\|_1$, where r_t is the measured root orientation (represented as a quaternion), r_t^* is the reference root orientation (represented as a quaternion).
- Root mean angular velocity error (E_{RLAE}): $\frac{1}{200 * 3} \sum_{t=1}^{200} \|\dot{r}_t - \dot{r}_t^*\|_1$

E.5. Tracking Metrics for Each Task

Table 5: Important hyperparameters of different algorithms in our experiments

Policy Parameter	Ours	DKRL	DKUC	DKAC	NNDM
Original space dimension	n' (35, 35, 35, 35, 45, 53, 53)	(35, 35, 35, 35, 45, 53, 53)	(35, 35, 35, 35, 45, 53, 53)	(35, 35, 35, 35, 45, 53, 53)	(35, 35, 35, 35, 45, 53, 53)
Control input dimension	m' (12, 12, 12, 12, 19, 23, 23)	(12, 12, 12, 12, 19, 23, 23)	(12, 12, 12, 12, 19, 23, 23)	(12, 12, 12, 12, 19, 23, 23)	(12, 12, 12, 12, 19, 23, 23)
Initial latent space dimension	$n^{(0)}$ (512, 384, 384, 535, 214, 222, 453)	(512, 384, 384, 535, 214, 222, 453)	(512, 384, 384, 535, 214, 222, 453)	(512, 384, 384, 535, 214, 222, 453)	(512, 384, 384, 535, 214, 222, 453)
Fixed step size	Δn 100	100	100	100	100
Inference horizon	H (16, 16, 16, 16, 24, 16, 16)	(16, 16, 16, 16, 24, 16, 16)	(16, 16, 16, 16, 24, 16, 16)	(16, 16, 16, 16, 24, 16, 16)	(16, 16, 16, 16, 24, 16, 16)
Initial training epochs	$J^{(0)}$ 100	100	100	100	100
Initial learning rate	1e-3	1e-3	1e-3	1e-3	1e-3
Network optimizer	Adam	Adam	Adam	Adam	Adam
Network scheduler	CosineAnnealingLR	CosineAnnealingLR	CosineAnnealingLR	CosineAnnealingLR	CosineAnnealingLR
Network hidden dimension	(256, 256, 256, 256, 256, 256)	(256, 256, 256, 256, 256, 256)	(256, 256, 256, 256, 256, 256)	(256, 256, 256, 256, 256, 256)	(512, 256, 256, 512, 256, 256, 512)
Network blocks number	(3, 3, 3, 3, 3, 3)	(3, 3, 3, 3, 3, 3)	(3, 3, 3, 3, 3, 3)	(3, 3, 3, 3, 3, 3)	(3, 3, 3, 3, 3, 3)
Discount Factor	0.99	0.99	0.99	0.99	0.99
Loss Weight	γ 0.1	0.1	0.1	0.1	0.1
Data normalization	α \checkmark	\checkmark	\checkmark	\checkmark	\checkmark
Initial trajectory length	l_{init} (100, 100, 100, 200, 100, 100, 200)	(100, 100, 100, 200, 100, 100, 200)	(100, 100, 100, 200, 100, 100, 200)	(100, 100, 100, 200, 100, 100, 200)	(100, 100, 100, 200, 100, 100, 200)
Clipped trajectory length	$l_{p^{(0)}}$ (16, 16, 16, 16, 24, 16, 16)	(16, 16, 16, 16, 24, 16, 16)	(16, 16, 16, 16, 24, 16, 16)	(16, 16, 16, 16, 24, 16, 16)	(16, 16, 16, 16, 24, 16, 16)
Reference trajectory length	l_r (500, 500, 500, 500, 500, 500, 500)	(500, 500, 500, 500, 500, 500, 500)	(500, 500, 500, 500, 500, 500, 500)	(500, 500, 500, 500, 500, 500, 500)	(500, 500, 500, 500, 500, 500, 500)
GMM cluster number	-	5	-	-	-

General Tracking Metrics								
Algorithm	Joint-relative ↓			Root-relative ↓				Survival ↑
	E_{JrPE}	E_{JrVE}	E_{JrAE}	E_{RPE}	E_{ROE}	E_{RLVE}	E_{RAVE}	T_{Sur}
Ours	0.0482	0.9047	52.9977	0.1645	0.0411	0.1409	0.3212	193.6900
DKRL	0.0801	1.2648	69.9505	0.2800	0.0565	0.2101	0.4657	180.5660
DKAC	0.2422	1.7859	69.4619	0.5077	0.2532	0.3533	0.7922	44.6020
DKUC	0.3137	1.4798	47.1150	0.5221	0.3251	0.3472	0.7125	27.9680
NNDM	0.1841	1.8721	75.2555	0.5357	0.2126	0.3564	0.7197	35.0360

Table 6: The average tracking metrics evaluated for each algorithm on Flat-Anymal-D.

General Tracking Metrics								
Algorithm	Joint-relative ↓			Root-relative ↓				Survival ↑
	E_{JrPE}	E_{JrVE}	E_{JrAE}	E_{RPE}	E_{ROE}	E_{RLVE}	E_{RAVE}	T_{Sur}
Ours	0.0282	0.6743	47.9247	0.0791	0.0218	0.0691	0.2273	191.3720
DKRL	0.0482	1.0185	70.5720	0.1139	0.0378	0.1008	0.3591	161.5880
DKAC	0.1462	3.8430	276.9420	0.3574	0.1101	0.2874	1.3771	10.8920
DKUC	0.0382	0.9525	69.6217	0.0997	0.0287	0.0896	0.3132	176.9560
NNDM	0.2166	3.9797	253.8551	0.4614	0.1215	0.3371	1.1712	3.8280

Table 7: The average tracking metrics evaluated for each algorithm on Flat-Unitree-A1.

General Tracking Metrics								
Algorithm	Joint-relative ↓			Root-relative ↓				Survival ↑
	E_{JrPE}	E_{JrVE}	E_{JrAE}	E_{RPE}	E_{ROE}	E_{RLVE}	E_{RAVE}	T_{Sur}
Ours	0.0404	0.8297	55.8780	0.1026	0.0376	0.0874	0.2689	185.5800
DKRL	0.0733	1.5231	104.3323	0.1803	0.0548	0.1424	0.4809	162.4500
DKAC	0.1710	2.9952	186.1956	0.3994	0.1956	0.2931	1.0813	19.5120
DKUC	0.1328	1.6218	89.0778	0.2163	0.1116	0.1814	0.5298	115.7020
NNDM	0.1716	3.3656	203.0976	0.4645	0.1290	0.3181	1.0053	4.6600

Table 8: The average tracking metrics evaluated for each algorithm on Flat-Unitree-Go2.

General Tracking Metrics								
Algorithm	Joint-relative ↓			Root-relative ↓				Survival ↑
	E_{JrPE}	E_{JrVE}	E_{JrAE}	E_{RPE}	E_{ROE}	E_{RLVE}	E_{RAVE}	T_{Sur}
Ours	0.0404	0.6152	36.8764	0.0838	0.1045	0.0928	0.3869	173.2980
DKRL	0.0760	1.0712	72.7223	0.1651	0.2369	0.1458	0.6009	92.9460
DKAC	0.1648	1.7733	91.0318	0.3195	0.4493	0.2015	0.7549	21.8420
DKUC	0.1177	0.8725	35.6163	0.1687	0.2227	0.1492	0.5043	82.0040
NNDM	0.1180	2.2806	147.1042	0.3023	0.4345	0.1997	0.8586	28.0060

Table 9: The average tracking metrics evaluated for each algorithm on Rough-Unitree-Go2.

General Tracking Metrics								
Algorithm	Joint-relative ↓			Root-relative ↓				Survival ↑
	E_{JrPE}	E_{JrVE}	E_{JrAE}	E_{RPE}	E_{ROE}	E_{RLVE}	E_{RAVE}	T_{Sur}
Ours	0.0185	0.2291	12.2077	0.0515	0.0254	0.0907	0.1729	193.2520
DKRL	0.1268	0.5842	21.4743	0.6188	0.2812	0.3165	0.6040	76.8560
DKAC	0.1951	0.9522	32.7991	0.3813	0.3077	0.2613	0.7258	40.0660
DKUC	0.1925	0.9012	32.0362	0.3701	0.2438	0.2563	0.6709	71.2460
NNDM	0.1105	0.8381	31.3497	0.4377	0.2752	0.2792	0.5807	109.2700

Table 10: The average tracking metrics evaluated for each algorithm on Flat-Unitree-H1.

General Tracking Metrics								
Algorithm	Joint-relative ↓			Root-relative ↓				Survival ↑
	E_{JrPE}	E_{JrVE}	E_{JrAE}	E_{RPE}	E_{ROE}	E_{RLVE}	E_{RAVE}	T_{Sur}
Ours	0.0162	0.3806	25.2465	0.0746	0.0403	0.1058	0.2487	190.1140
DKRL	0.0860	1.1300	55.0856	0.5007	0.2195	0.3090	0.6073	73.5960
DKAC	0.1819	2.0094	110.0289	0.3974	0.3332	0.3274	0.9012	14.0400
DKUC	0.1579	0.9549	44.7592	0.3077	0.2420	0.2746	0.6048	51.1280
NNDM	0.1158	1.5910	87.3439	0.4060	0.2896	0.2994	0.7254	37.4180

Table 11: The average tracking metrics evaluated for each algorithm on Flat-Unitree-G1.

General Tracking Metrics								
Algorithm	Joint-relative ↓			Root-relative ↓				Survival ↑
	E_{JrPE}	E_{JrVE}	E_{JrAE}	E_{RPE}	E_{ROE}	E_{RLVE}	E_{RAVE}	T_{Sur}
Ours	0.0291	0.4723	28.8812	0.1684	0.1161	0.1971	0.4790	157.2460
DKRL	0.0915	1.1179	78.8252	0.4449	0.2194	0.2808	0.6910	76.4780
DKAC	0.1699	1.1268	56.4011	0.4061	0.2754	0.2979	0.7680	24.2240
DKUC	0.1503	0.7970	35.7952	0.3692	0.2186	0.2779	0.5559	52.2300
NNDM	0.0905	1.4870	94.1604	0.4262	0.2918	0.3075	0.9143	30.0780

Table 12: The average tracking metrics evaluated for each algorithm on Rough-Unitree-G1.

